Nano World Journal

https://doi.org/10.17756/nwj.2026-149

Research Article

Open Access

Two Dopants, Two Behaviours: Unlocking the Structural Duality of Bismuth(III) Oxide-zinc oxide and Calcium Oxide-zinc oxide Nanocomposites

A.L. Subramaniyan*

School of Engineering, Alliance University, Karnataka, India

***Correspondence to:**
A.L. Subramaniyan
School of Engineering,
Alliance University,
Karnataka, India.
E-mail: subramaniyan.al@alliance.edu.in

Received: December 18, 2025
Accepted: February 20, 2026
Published: February 25, 2026

Citation: Subramaniyan AL. 2026. Two Dopants, Two Behaviours: Unlocking the Structural Duality of Bismuth(III) Oxide-zinc oxide and Calcium Oxide-zinc oxide Nanocomposites. *NanoWorld J* 12(1): 1-7.

Copyright: © 2026 Subramaniyan. This is an Open Access article distributed under the terms of the Creative Commons Attribution 4.0 International License (CCBY) (http://creativecommons.org/licenses/by/4.0/) which permits commercial use, including reproduction, adaptation, and distribution of the article provided the original author and source are credited.

Published by United Scientific Group

Abstract

Zinc oxide (ZnO) continues to attract considerable attention due to its structural versatility and tunable properties at the nanoscale. Modification of ZnO through metal-oxide incorporation provides an effective strategy to control crystallinity, defect density, and microstructural evolution. In the present work, ZnO, calcium oxide (CaO)-ZnO, and bismuth(III) oxide (Bi_2O_3)-ZnO nanocomposites were synthesized via a simple sol-gel route using zinc sulphate ($ZnSO_4$), calcium nitrate ($Ca(NO_3)_2$), and bismuth sulphate ($Bi_2(SO_4)_3$) precursors, followed by calcination at 400 °C. Structural and morphological characteristics were systematically investigated using X-ray diffraction (XRD), scanning electron microscopy (SEM), and Fourier-transform infrared spectroscopy (FTIR). XRD analysis confirmed the formation of crystalline wurtzite ZnO in all samples, with additional diffraction features corresponding to CaO and Bi_2O_3 in the respective composites. Incorporation of CaO resulted in reduced crystallite size and increased lattice disorder, indicating effective grain-growth suppression, whereas Bi_2O_3 incorporation promoted crystallite coarsening and enhanced crystallinity. SEM observations revealed anisotropic Bi_2O_3 microstructures embedded within the ZnO matrix, while CaO-ZnO samples exhibited densely agglomerated assemblies of nanoscale primary particles. FTIR spectra further verified the presence of characteristic metal-oxygen vibrational modes and surface-associated functional groups, supporting the structural conclusions drawn from XRD. The results demonstrate that dopant chemistry plays a decisive role in governing the nanoscale structural evolution of ZnO under identical synthesis conditions. This study establishes a clear structure-composition relationship in ZnO-based oxide nanocomposites and provides a reliable framework for further investigations aimed at controlled microstructural tailoring.

Keywords

Zinc oxide nanostructures, Bismuth oxide-zinc oxide, Calcium oxide-zinc oxide, Sol-gel synthesis, Crystallinity, Agglomeration, Nanocomposites

Introduction

ZnO is a well-established multifunctional material owing to its exceptional physicochemical, mechanical, thermal, optical, and electrical properties. Nanoscale ZnO further enhances these characteristics by enabling size- and shape-dependent tunability of functional behaviour [1]. The proportion of publications focusing specifically on nano-ZnO has increased significantly—by 14.7% between 2011 and 2020—demonstrating the rapid expansion of research activity in this domain [2]. A comprehensive review covering 92 years of ZnO research further underscores its technological importance and highlights nano-ZnO as the most prominent semiconducting oxide at present [3].

Considerable research has therefore been directed toward synthesizing doped ZnO nanoparticles to meet application-specific requirements. Transition metals, rare-earth elements, and various other metallic dopants have been incorporated into ZnO matrices to introduce enhanced magnetic, photocatalytic, and chemical functionalities. Doped ZnO has also gained attention for biomedical applications, including imaging, antitumor treatments, and antibacterial activity [4].

Bismuth, a heavy metal with versatile chemical behaviour, is widely utilized in nanocomposite synthesis for energy and environmental applications [5]. At the nanoscale, bismuth exhibits unique physiochemical properties distinct from its bulk counterpart, particularly contributing to improved photocatalytic performance in composite systems. Bi_2O_3 nanoparticles additionally offer broad application potential while exhibiting comparatively lower adverse effects [6]. CaO nanoparticles have similarly attracted interest for catalysis, water purification, adsorption, and antibacterial applications [7]. Their non-toxic nature, low cost, and reusability make CaO-based catalytic materials particularly attractive.

Nanocomposites, defined as multiphase materials in which at least one constituent exists within the 1-100 nm range, can be developed with metallic, polymeric, or ceramic matrices combined with nanoscale fillers to achieve tailored functionalities. Ceramic-matrix nanocomposites, in particular, are valued for their chemical stability, heat resistance, and enhanced fracture toughness, although often at the expense of reduced stiffness. The growing scientific interest in such materials is reflected by the publication of nearly 20,000 papers related to nanocomposites in 2019 alone [8].

Bi_2O_3-ZnO nanocomposites have previously been synthesized through sonochemical routes and applied successfully in electrochemical sensing technologies [9]. Bismuth-doped ZnO nanoparticles have also been prepared via sol-gel methods using acetate precursors, followed by calcination at 500 °C [10]. In the present work, an alternative approach is explored by synthesizing Bi_2O_3-ZnO nanocomposites through a simple sol-gel route employing sulphate-based precursors. Additionally, while CaO-ZnO nanocomposites have recently been produced via sol-gel synthesis using calcium chloride and zinc acetate precursors for combating drug-resistant *Candida auris*, the present study introduces a modified precursor system based on $Ca(NO_3)_2$ and $ZnSO_4$.

Materials and Methods

The stating materials used for the synthesis if the bimetallic oxide nanocomposite are $ZnSO_4$ heptahydrate ($ZnSO_4 \cdot 7H_2O$, Spectrum Reagents, Cochin, India; LR grade, 99%), $Ca(NO_3)_2$, (Kemphasol, Bombay, India; AR grade, 98%), ($Bi_2(SO_4)_3$, Hi-Pure, Chennai, India), and sodium hydroxide pellets (NaOH, AR grade). Deionized water was employed throughout the synthesis.

Synthesis of ZnO nanoparticles

ZnO nanoparticles were synthesized via a conventional sol-gel route using $ZnSO_4$ precursor.

$ZnSO_4 \cdot 7H_2O$ (0.564 g, 1.96×10^{-3} mol) was dissolved in 100 mL of deionized water under magnetic stirring for 30 min, resulting in a 0.0196 M Zn^{2+} solution.

NaOH pellets were added dropwise under continuous stirring to achieve hydrolysis and condensation. A total of 0.157 g NaOH (3.92×10^{-3} mol) was added, corresponding to a Zn^{2+}:OH^- molar ratio of 1:2, sufficient for complete precipitation of zinc hydroxide. The pH of the sol was carefully monitored and maintained in the range of pH = 11.5.

Stirring was continued for 2.5 h until a homogeneous milky white sol was obtained. The sol was aged at room temperature for 120 h to promote structural reorganization and gel maturation. The aged gel was dried and subsequently calcined in a muffle furnace at 400 °C for 3 h, employing a controlled heating rate of 5 °C min^{-1}. After calcination, the samples were allowed to cool naturally inside the furnace, cooling approximately 3 °C min^{-1}. The resulting dried mass was hand-milled for 10 min to obtain fine white ZnO nanopowders.

Synthesis of CaO-ZnO nanocomposites

CaO-ZnO nanocomposites were synthesized using the same sol-gel protocol. $ZnSO_4 \cdot 7H_2O$ (0.564 g, 1.96×10^{-3} mol) and $Ca(NO_3)_2$ (0.236 g, 1.44×10^{-3} mol) were dissolved together in 100 mL of deionized water and stirred for 30 min. This corresponds to a Ca^{2+}:Zn^{2+} molar ratio of 0.73:1 (≈ 42 mol% CaO with respect to total metal cations).

NaOH pellets (0.31 g, 7.75×10^{-3} mol) were added gradually to maintain a total metal ion:OH^- ratio ≈ 1:2, ensuring complete hydroxide formation. The pH was adjusted and stabilized at 11.5. Stirring was continued for 2.5 h until a thick white sol formed.

The sol was aged at ambient conditions for 120 h, followed by calcination at 400 °C for 3 h using a heating rate of 5 °C/min. Furnace cooling was employed to avoid thermal shock. The calcined powders were hand-milled for 10 min, yielding dull white CaO-ZnO nanocomposites. The selected calcination temperature favors controlled crystallite growth and phase stabilization in ZnO-based systems [11].

Synthesis of Bi_2O_3-ZnO nanocomposites

Bi_2O_3-ZnO nanocomposites were prepared by replacing $Ca(NO_3)_2$ with $Bi_2(SO_4)_3$ while maintaining identical synthesis conditions.

$ZnSO_4 \cdot 7H_2O$ (0.564 g, 1.96×10^{-3} mol) and $Bi_2(SO_4)_3$ (0.706 g, 1.51×10^{-3} mol) were dissolved in 100 mL of deionized water. Considering two Bi^{3+} ions per formula unit, the effective Bi^{3+}:Zn^{2+} molar ratio was 1.54:1.

NaOH pellets (0.45 g, 1.13×10^{-2} mol) were added dropwise to ensure complete precipitation, maintaining the solution pH at 11.5. The sol was stirred for 2.5 h, aged for 120 h, and calcined at 400 °C for 3 h using the same heating (5 °C min^{-1}) and furnace-cooling protocol as applied to ZnO and CaO-ZnO samples. All powders were finally hand-milled for uniformity.

Characterization techniques

Structural analysis was carried out by XRD (Bruker ECO D8 Advance) with copper (Cu) Kα radiation (λ = 1.540 Å), operating over a 2θ range of 10° - 80°, step size of 0.020°, and a step time of 32 s. Surface morphology was examined using SEM, Carl Zeiss EVO 18 at an accelerating voltage of 20 kV and a magnification of 10.00 kx. FTIR spectra were recorded using a Shimadzu IRTracer-100 spectrometer in the range 500 - 4000 cm^{-1}, with a signal-to-noise ratio of 60,000 and a high-speed scan rate of 20 spectra/s.

Results and Discussion

XRD analysis

In figure 1 which indicates XRD of ZnO nanopowder, the weak and broad features observed between 20° and 30° do not correspond to any intense reflections of hexagonal wurtzite ZnO. These low-intensity peaks are attributed to secondary or residual phases, primarily originating from incompletely decomposed sulphate species ($ZnSO_4$-related complexes) or transient zinc hydroxysulphate intermediates formed during the sol-gel process. At a relatively low calcination temperature of 400 °C, trace sulphate groups may not be fully eliminated, leading to weak diffraction signatures in this region. The broad nature of these peaks also indicates poorly crystalline or amorphous remnants, rather than well-defined crystalline impurity phases.

In doped samples, similar low-angle features (<30°) may additionally arise from strain-induced lattice distortion, short-range ordering, or the presence of dopant oxide clusters that do not form long-range crystalline order.

The prominent diffraction peaks at 2θ ≈ 31.8° (100), 34.4° (002), 36.3° (101), 47.5° (102), 56.6° (110), 62.9° (103), 66.4° (200), and 69.1° (201) confirm the formation of hexagonal wurtzite ZnO, in agreement with standard Joint Committee on Powder Diffraction Standards cards [12, 13].

The lattice parameters a and c were calculated using the hexagonal lattice relation:

$$\frac{1}{d^2} = \frac{4}{3}\left(\frac{h^2 + hk + k^2}{a^2}\right) + \frac{l^2}{c^2}$$

Using the (100) and (002) reflections:

For (100): $a = \frac{2}{\sqrt{3}} d_{100}$

For (002): $c = 2d_{002}$

The calculated lattice parameters were found to be:

a ≈ 3.24 Å

c ≈ 5.20 Å

These values are in close agreement with standard ZnO lattice constants (a = 3.249 Å, c = 5.206 Å), indicating minimal lattice distortion in undoped ZnO and good phase purity.

Crystallite size estimation

The average crystallite size was estimated using the Debye-Scherrer equation:

$$D = \frac{0.91\lambda}{\beta \cos\theta}$$

Where λ = 1.540 Å (Cu K_α radiation), β is the full width at half maximum of the (101) reflection (corrected for instrumental broadening), θ is the Bragg angle.

The calculated average crystallite sizes were:

ZnO: ~24 nm

CaO-ZnO: ~18 nm

Bi_2O_3-ZnO: ~56 nm

The observed peak broadening in ZnO and CaO-ZnO confirms their nanocrystalline nature.

CaO-ZnO nanocomposite: lattice distortion and grain refinement

In figure 2, the retention of ZnO diffraction peaks confirms that the wurtzite structure is preserved upon CaO incorporation. Additional peaks at ~29°, 37°, 43°, 54°, and 64° correspond to crystalline CaO, confirming composite formation.

The reduction in intensity of the ZnO (101) peak and the relative enhancement of the (100) reflection indicate anisotropic strain and lattice distortion, caused by partial substitution of Ca^{2+} (ionic radius ~1.00 Å) for Zn^{2+} (0.74 Å).

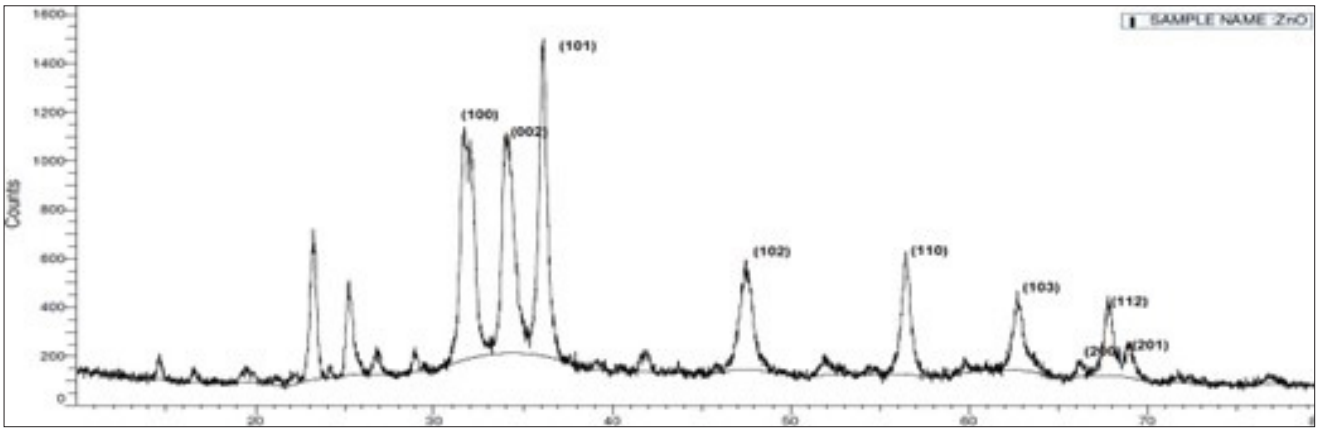

Figure 1: XRD pattern of ZnO nanopowder.

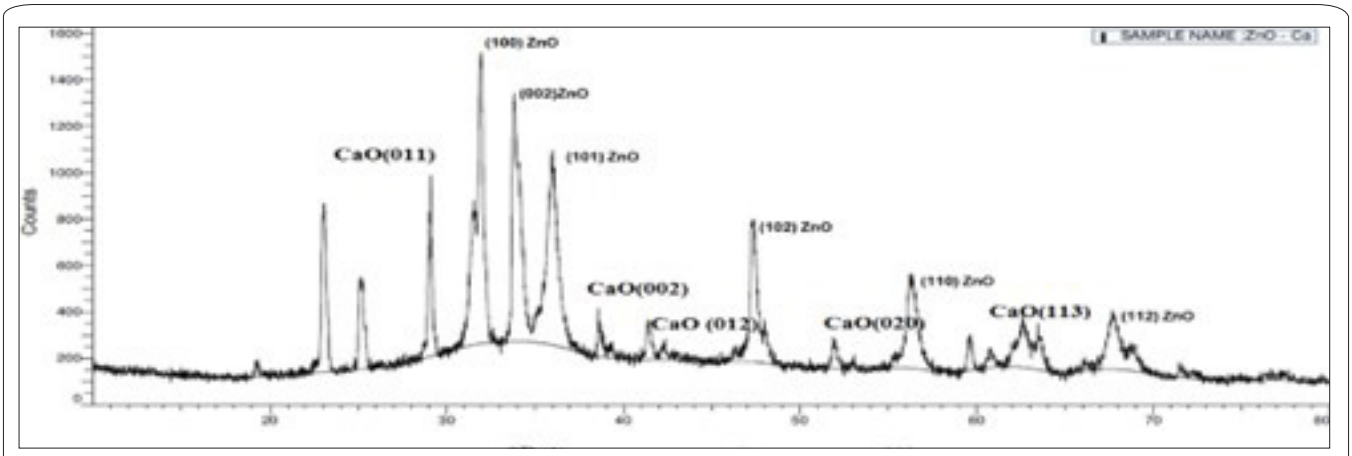

Figure 2: XRD pattern of CaO-ZnO nanocomposite.

This size mismatch introduces point defects and inhibits grain boundary mobility, resulting in suppressed grain growth and a reduced crystallite size (18 nm). Such refinement is consistent with defect-mediated grain pinning effects [14].

Figure 3 shows the ZnO wurtzite reflections along with a distinct peak near $2\theta \approx 27^{\circ}$, characteristic of monoclinic α-Bi_2O_3, the thermodynamically stable polymorph at room temperature. Depending on synthesis conditions, Bi_2O_3 can exist in several polymorphic forms:

α-Bi_2O_3 (monoclinic, stable below 730 °C)

β-Bi_2O_3 (tetragonal, metastable)

γ-Bi_2O_3 (body-centered cubic)

δ-Bi_2O_3 (face-centered cubic, stable above 730 °C)

The presence of the α-Bi_2O_3 phase indicates successful formation of the Bi_2O_3-ZnO composite without high-temperature phase transformation.

The pronounced suppression of the ZnO (101) peak and enhancement of the (100) peak in Bi_2O_3-ZnO suggest strong interfacial interaction and altered growth kinetics induced by Bi^{3+} ions. The larger ionic radius and higher atomic mass of Bi promote enhanced atomic diffusion, facilitating grain coarsening during calcination.

The degree of crystallinity was estimated using the area method:

$$\text{Crystallinity (\%)} = \frac{A_c}{A_c + A_a} \times 100$$

Where A_c is the integrated area under crystalline diffraction peaks, and A_a is the area corresponding to the amorphous background.

Using background-subtracted XRD profiles, the Bi_2O_3-ZnO nanocomposite exhibited:

Crystalline peak area ≈ 78%

Amorphous contribution ≈ 22%

The higher crystallinity of Bi_2O_3-ZnO compared to ZnO and CaO-ZnO reflects improved structural ordering and enhanced grain growth, consistent with the observed increase in crystallite size.

The increase in crystallite size from 24 nm (ZnO) to 56 nm (Bi_2O_3-ZnO) indicates that Bi_2O_3 acts as a grain-growth promoter, enhancing atomic mobility during heat treatment. In contrast, CaO suppresses grain growth, resulting in refined crystallites (18 nm).

These contrasting behaviours are technologically significant:

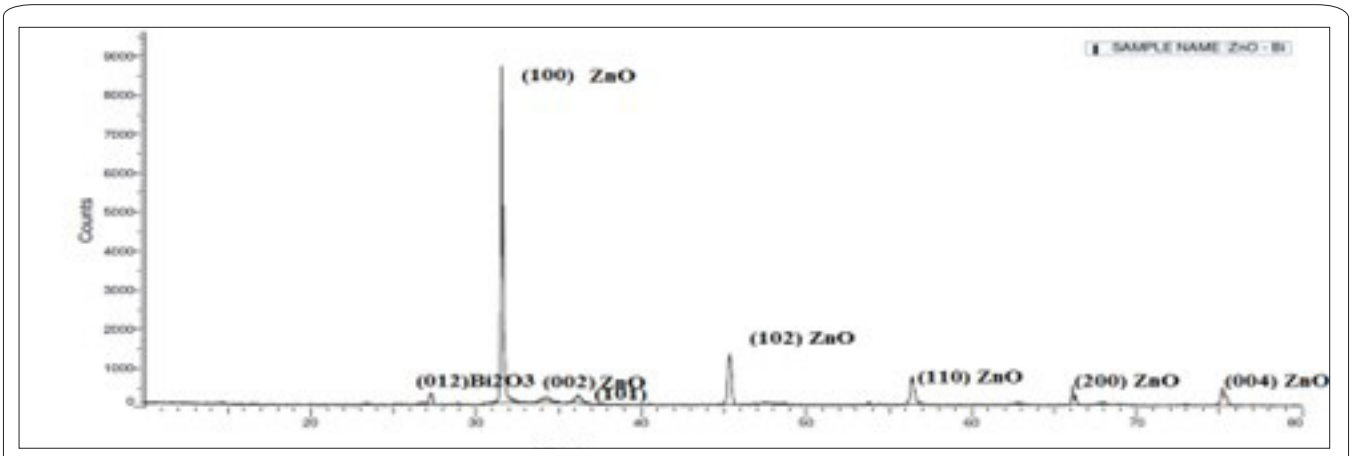

Figure 3: XRD pattern of Bi_2O_3-ZnO nanocomposite.

Bi_2O_3-ZnO, with larger grains and higher crystallinity, is suitable for high-temperature and creep-resistant applications.

CaO-ZnO, with finer grains and higher defect density, offers improved fatigue resistance and cyclic stability.

SEM analysis

Figure 4 shows the SEM micrograph of the CaO-ZnO nanocomposite. The image reveals highly agglomerated clusters with apparent particle sizes ranging from approximately 15 nm to 3000 nm. This wide size distribution does not represent individual crystallite dimensions but rather the formation of secondary particles (agglomerates) composed of nanoscale primary crystallites.

The significant agglomeration observed in CaO-ZnO is a well-known phenomenon in oxide nanoceramics and arises from several concurrent mechanisms. First, both ZnO and CaO possess high surface energies, which promote strong interparticle attractive forces such as van der Waals interactions and electrostatic forces. During solvent evaporation and gel drying, capillary stresses pull neighbouring nanoparticles together, leading to irreversible hard agglomerates. These agglomerates persist even after calcination and mild mechanical milling.

Second, the relatively low calcination temperature (400 °C), while effective in preserving nanoscale crystallites, is insufficient to induce complete neck dissolution or grain boundary separation. Instead, Ostwald ripening and partial coalescence occur, whereby smaller crystallites dissolve and redeposit onto larger ones within an agglomerate, strengthening cluster formation without significant crystallite growth. This interpretation is fully consistent with the XRD-derived crystallite size of ~18 nm, which reflects the coherent diffracting domain rather than the physical particle size observed in SEM.

Importantly, the presence of visible grain boundaries inside the agglomerated clusters confirms that the micro-sized features are assemblies of nanoscale units rather than single large crystals. Thus, the apparent micron-sized particles in SEM are secondary agglomerates, while the primary particles remain nanocrystalline in nature [15].

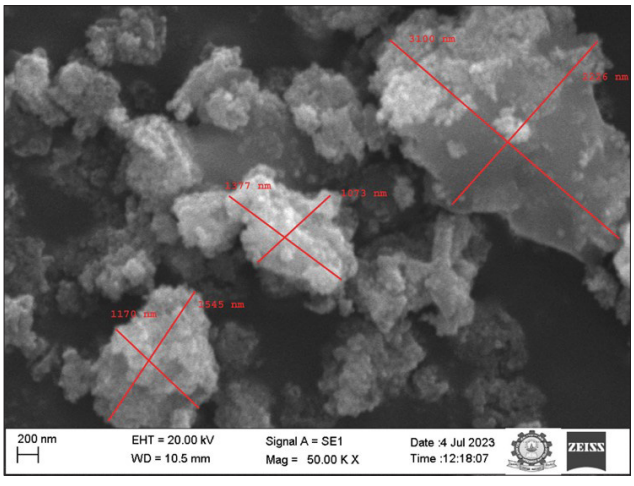

Figure 4: SEM image of CaO-ZnO nanocomposite.

Figure 5 displays the SEM micrograph of the Bi_2O_3-ZnO nanocomposite. In contrast to CaO-ZnO, the microstructure exhibits well-defined rectangular and rod-like Bi_2O_3 grains, with widths ranging from 100 to 300 nm, embedded within the ZnO matrix. The formation of such anisotropic structures indicates directional nucleation and growth, characteristic of Bi_2O_3 polymorphs with lower symmetry.

The rod-like morphology suggests that Bi_2O_3 undergoes oriented crystal growth, driven by anisotropic surface energies of specific crystallographic planes. This behaviour is consistent with the enhanced crystallinity and larger crystallite size (~56 nm) observed in XRD. The clear phase boundaries between Bi_2O_3 rods and the ZnO matrix indicate phase separation rather than complete lattice substitution, in agreement with the presence of distinct Bi_2O_3 reflections in the XRD pattern.

Furthermore, the higher atomic mass and larger ionic radius of Bi^{3+} enhance atomic mobility during calcination, promoting grain coarsening and morphological evolution. As a result, Bi_2O_3 acts as a grain-growth promoter, in contrast to CaO, which suppresses grain growth through defect pinning.

The apparent discrepancy between XRD crystallite sizes (18 - 56 nm) and SEM particle sizes (up to 3000 nm) is therefore not contradictory but expected. XRD measures the size of coherently diffracting crystalline domains, whereas SEM reveals the physical size of particle agglomerates. In nanoceramic systems, strong interparticle interactions during sol-gel processing, drying, and calcination result in hierarchical structures where nanoscale crystallites assemble into micro-scale agglomerates.

Such multiscale organization has been widely reported for ZnO-based nanocomposites and is particularly pronounced in alkaline synthesis routes employing NaOH, where rapid nucleation generates large numbers of fine crystallites with a strong tendency to aggregate [16, 17].

FTIR analysis

Figure 6 displays the FTIR spectrum of the CaO-ZnO nanocomposite. A broad and intense band observed at ~3510 - 3420 cm^{-1} corresponds to O-H stretching vibrations, while the

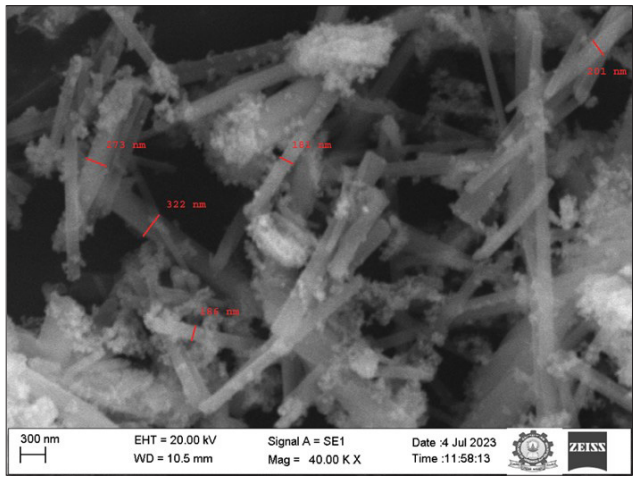

Figure 5: SEM image of Bi_2O_3-ZnO nanocomposite.

band near ~1430 cm^{-1} is associated with O-H bending modes. The enhanced intensity of these bands compared to pure ZnO indicates increased surface hydroxylation and defect density, which correlates with the reduced crystallite size (~18 nm) and increased lattice distortion inferred from XRD analysis.

The absorption band at ~877 cm^{-1} is attributed to C-H bending vibrations, and the weak band near ~2910 cm^{-1} corresponds to C-H stretching modes, likely due to trace carbonate species adsorbed on the nanoparticle surface. The

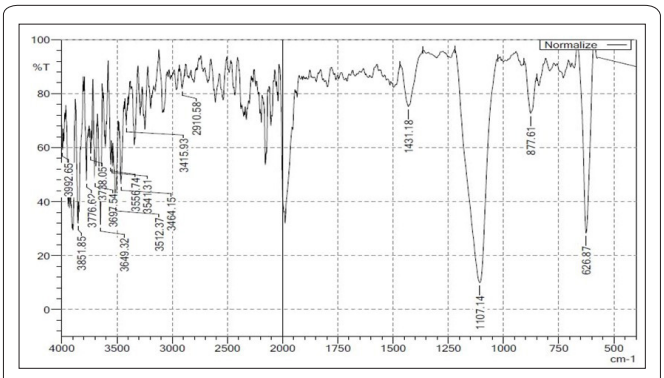

Figure 6: FTIR spectra of CaO-ZnO composite.

band at ~1107 cm^{-1} is assigned to C-O stretching vibrations, supporting the presence of residual carbonate or nitrate-derived species. These residual vibrational features are consistent with the suppressed intensity and broadening of ZnO diffraction peaks, particularly the (101) plane, observed in XRD, indicating incomplete lattice ordering due to Ca incorporation.

The overlapping Zn-O and Ca-O vibrational modes in the low-frequency region (<700 cm^{-1}) further support the composite nature of the material, in agreement with the additional CaO-related diffraction peaks identified in the XRD pattern.

The FTIR spectrum of the Bi_2O_3-ZnO nanocomposite (Figure 7) exhibits a broad O-H stretching band in the 3100-3500 cm^{-1} region [18], though with comparatively reduced intensity relative to CaO-ZnO. This reduction reflects lower surface defect density, consistent with the higher crystallinity (~78%) and larger crystallite size (~56 nm) obtained from XRD analysis.

A distinct absorption band near ~619 cm^{-1} is attributed to Bi-O stretching vibrations, confirming the presence of Bi_2O_3 within the composite [19]. The coexistence and partial overlap of Zn-O and Bi-O vibrational modes in this region correlate directly with the dual-phase nature revealed by XRD, where characteristic reflections of both wurtzite ZnO and α-Bi_2O_3 were observed.

Weak absorption bands in the 1400 - 1000 cm^{-1} region are present but significantly attenuated compared to CaO-ZnO, indicating more effective removal of precursor-derived residues. This observation is consistent with the sharper XRD peaks and higher crystallinity, suggesting improved lattice ordering and reduced structural disorder in the Bi_2O_3-ZnO system.

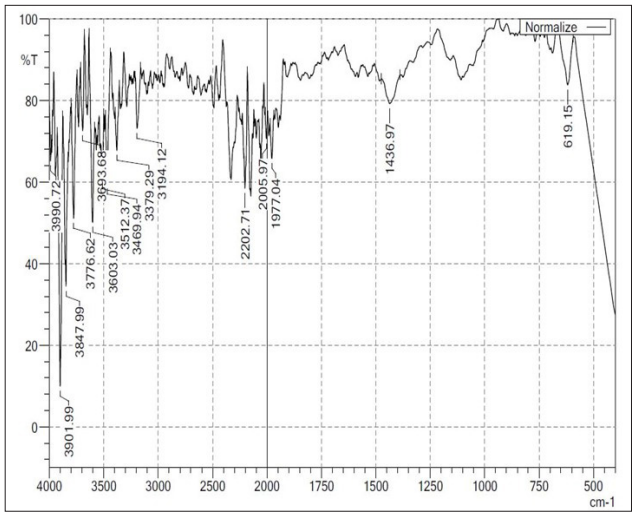

Figure 7: FTIR Spectra of Bi_2O_3-ZnO nanocomposite.

A comparative evaluation of FTIR spectra reveals systematic variations in vibrational band intensity and bandwidth that correlate strongly with XRD-derived structural parameters. The increase in hydroxyl and carbonate-related FTIR band intensity in CaO-ZnO aligns with XRD evidence of smaller crystallite size, peak broadening, and lattice distortion, indicating enhanced defect concentration. In contrast, the suppressed hydroxyl absorption and sharper metal-oxygen vibrational bands in Bi_2O_3-ZnO correlate with larger crystallite size, higher crystallinity, and well-defined diffraction peaks.

Thus, FTIR analysis complements XRD results by providing insight into surface chemistry and short-range bonding, confirming that CaO incorporation promotes defect formation and lattice disorder, while Bi_2O_3 enhances structural ordering and crystallinity. The combined FTIR-XRD interpretation offers a coherent understanding of phase formation, defect evolution, and crystallographic stability in the synthesized nanocomposites.

Conclusion

ZnO, CaO-ZnO, and Bi_2O_3-ZnO nanostructured materials were successfully synthesized via a simple and reproducible sol-gel route using $ZnSO_4$, $Ca(NO_3)_2$, and $Bi_2(SO_4)_3$ as precursor salts. XRD analysis confirmed the formation of crystalline wurtzite ZnO in all samples, with additional reflections corresponding to CaO and Bi_2O_3 phases in the respective composites, indicating successful composite formation without secondary phase suppression of ZnO.

Crystallite size analysis revealed nanoscale dimensions in the range of 24 - 56 nm. Incorporation of CaO resulted in a reduction of ZnO crystallite size and increased peak broadening, indicating enhanced lattice distortion and defect concentration. In contrast, Bi_2O_3 incorporation promoted crystallite growth and improved lattice ordering, as evidenced by sharper diffraction peaks and higher estimated crystallinity. These observations confirm that CaO and Bi_2O_3 exert contrasting influences on the structural evolution of ZnO,

acting respectively as grain-growth inhibitors and promoters under identical synthesis conditions.

FTIR spectroscopy corroborated the XRD findings by revealing distinct metal-oxygen vibrational modes associated with Zn-O, Ca-O, and Bi-O bonds. Variations in hydroxyl- and carbonate-related band intensities across the samples were consistent with differences in crystallite size and structural disorder inferred from XRD, providing complementary insight into short-range bonding and surface chemistry.

SEM observations showed that Bi_2O_3-ZnO exhibits well-defined anisotropic Bi_2O_3 morphologies embedded within the ZnO matrix, while CaO-ZnO forms highly agglomerated assemblies of nanoscale primary particles. These morphological features are consistent with the phase-separated nature and crystallinity trends revealed by diffraction analysis.

Overall, the results demonstrate that controlled incorporation of alkaline-earth and heavy-metal oxides into ZnO via a sol-gel route provides an effective means to tailor crystallite size, lattice order, and phase composition. The present work establishes a clear structure-composition relationship in ZnO-based oxide nanocomposites, serving as a foundation for future investigations into property optimization through systematic compositional and processing control.

Acknowledgements

None.

Conflict of Interest

None.

References

1. Babayevska N, Przysiecka Ł, Iatsunskyi I, Nowaczyk G, Jarek M, et al. 2022. ZnO size and shape effect on antibacterial activity and cytotoxicity profile. *Sci Rep* 12(1): 1-13. https://doi.org/10.1038/s41598-022-12134-3
2. Wojnarowicz J, Chudoba T, Lojkowski W. 2020. A review of microwave synthesis of zinc oxide nanomaterials: reactants, process parameters and morphologies. *Nanomaterials (Basel)* 10(6): 1086. https://doi.org/10.3390/nano10061086
3. Sharma P, Hasan MR, Mehto NK, Deepak, Bishoyi A, et al. 2022. 92 years of zinc oxide: has been studied by the scientific community since the 1930s- an overview. *Sens Int* 3: 100182. https://doi.org/10.1016/j.sintl.2022.100182
4. Carofiglio M, Barui S, Cauda V, Laurenti M. 2020. Doped zinc oxide nanoparticles: synthesis, characterization and potential use in nanomedicine. *Appl Sci (Basel)* 10(15): 5194. https://doi.org/10.3390/app10155194
5. Sivasubramanian PD, Chang JH, Nagendran S, Dong CD, Shkir M, et al. 2022. A review on bismuth-based nanocomposites for energy and environmental applications. *Chemosphere* 307(Pt 1): 135652. https://doi.org/10.1016/j.chemosphere.2022.135652
6. Flayyih AO, Mahdi WK, Abu Zaid YIM, Falih H. 2022. Biosynthesis, characterization, and applications of bismuth oxide nanoparticles using aqueous extract of *Beta vulgaris*. *Chem Methodol* 6(8): 620-628. https://doi.org/10.22034/chemm.2022.342124.1522
7. Jadhav V, Bhagare A, Wahab S, Lokhande D, Vaidya C, et al. 2022. Green synthesized calcium oxide nanoparticles using *Moringa oleifera* leaf extract and antibacterial activity. *J Nanomater* 2022: 1-7. https://doi.org/10.1155/2022/9047507
8. Carrola M, Asadi A, Zhang H, Papageorgiou DG, Bilotti E, et al. 2021. Synergistically derived material properties via additive manufacturing of nanocomposites. *Adv Funct Mater* 31(46): 2103334. https://doi.org/10.1002/adfm.202103334
9. Ansari S, Ansari MS, Satsangee SP, Jain R. 2021. Bi_2O_3/ZnO nanocomposite: synthesis, characterization and electrochemical detection of balofloxacin as an anti-biotic drug. *J Pharm Anal* 11(1): 57-67. https://doi.org/10.1016/j.jpha.2020.03.013
10. Boumezoued A, Guergouri K, Barille R, Rechem D, Zaabat M, et al. 2019. ZnO nanopowders doped with bismuth oxide, from synthesis to electrical application. *J Alloys Compd* 791: 550-558. https://doi.org/10.1016/j.jallcom.2019.03.251
11. Radingoana PM, Guillemet-Fritsch S, Olubambi PA, Chevallier G, Estournès C. 2019. Influence of processing parameters on the densification and the microstructure of pure zinc oxide ceramics prepared by spark plasma sintering. *Ceram Int* 45(8): 10035-10043. https://doi.org/10.1016/j.ceramint.2019.02.048
12. Reda AE, Fayed B. 2023. The synthesis of calcium doped zinc oxide ceramic nanoparticles via sol-gel effective against the emerging multi-drug-resistant *Candida auris*. *J Aust Ceram Soc* 59: 1315-1323. https://doi.org/10.1007/s41779-023-00912-9.
13. Zhou J, Zhao F, Wang Y, Zhang Y, Yang L. 2007. Size-controlled synthesis of ZnO nanoparticles and photoluminescence properties. *J Lumin* 122-123: 195-197. https://doi.org/10.1016/j.jlumin.2006.01.089
14. Tayyaba S, Ashraf MW, Tariq MI, Akhlaq M, Balas VE, et al. 2020. Simulation, analysis, and characterization of calcium-doped ZnO nanostructures for dye-sensitized solar cells. *Energies* 13(18): 4863. https://doi.org/10.3390/en13184863.
15. Elshayb OM, Farroh KY, Amin HE, Atta AM. 2021. Green synthesis of zinc oxide nanoparticles: fortification for rice grain yield and nutrients uptake enhancement. *Molecules* 26(3): 584. https://doi.org/10.3390/molecules26030584
16. Thanh NT, Maclean N, Mahiddine S. 2014. Mechanisms of nucleation and growth of nanoparticles in solution. *Chem Rev* 114(15): 7610-7630. https://doi.org/10.1021/cr400544s
17. Cölfen H, Antonietti M. 2013. Kinetics and mechanisms of aggregative nanocrystal growth. Chem Mater 26(1): 1-21. https://doi.org/10.1021/cm402139r
18. Motakef-Kazemi N, Yaqoubi M. 2020. Green synthesis and characterization of bismuth oxide nanoparticles using *Mentha pulegium* extract. *Iran J Pharm Res* 19(2): 70-79. https://doi.org/10.22037/ijpr.2019.15578.13190
19. Labib S. 2017. Preparation, characterization and photocatalytic properties of doped and undoped Bi_2O_3. *J Saudi Chem Soc* 21(6): 664-672. https://doi.org/10.1016/j.jscs.2015.11.003